ACS APPLIED MATERIALS & INTERFACES

Research Article

www.acsami.org

A New Oxyfluorinated Titanium Phosphate Anode for A High-Energy Lithium-Ion Battery

Zhaohui Ma,[†] Chunwen Sun,*[,†] Yingchun Lyu,[†] Yuesheng Wang,[†] Youngsik Kim,[‡] and Liquan Chen[†]

[†]Key Laboratory for Renewable Energy, Beijing Key Laboratory for New Energy Materials and Devices, Beijing National Laboratory for Condensed Matter Physics, Institute of Physics, Chinese Academy of Sciences, Beijing 100190, China

[‡]Interdisciplinary School of Green Energy, Ulsan National Institute of Science and Technology, Ulsan, Korea

Supporting Information

ABSTRACT: $Na_3[Ti_2P_2O_{10}F]$ was synthesized by a hydrothermal method. It has an open framework structure consisting of $TiFO_5$ octahedra and PO_4 tetrahedra. The feasibility of $Na_3[Ti_2P_2O_{10}F]$ as an anode material for lithium-ion batteries was first studied. $Na_3[Ti_2P_2O_{10}F]$ exhibits a reversible capacity of more than 200 mAh g^{-1} at a discharge/charge current rate of 20 mA g^{-1} (~0.1 C) and 105 mA g^{-1} at a discharge/charge current rate of 400 mA g^{-1} (~2 C) with a lower intercalation voltage. The result of in situ X-ray diffraction test shows the structural evolution during the first discharge/charge cycle. The structure of $Na_3[Ti_2P_2O_{10}F]$ was kept during discharge/charge with a slight change of the lattice parameters, which indicates a lithium solid solution behavior.

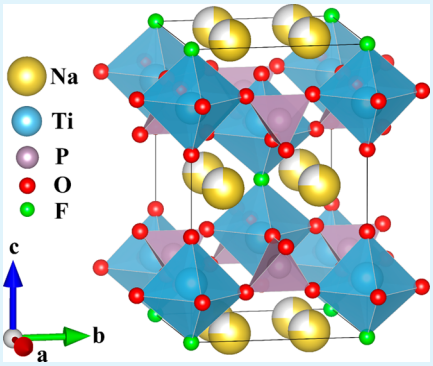

KEYWORDS: *$Na_3[Ti_2P_2O_{10}F]$, lithium-ion battery, anode material, structural evolution*

1. INTRODUCTION

Lithium-ion batteries (LIBs) have been one of the most dominant energy-storage technologies due to the high energy density and environmental benignity.[1−3] Graphite has been used as a main anode in rechargeable LIBs for more than 30 years via a Li intercalation mechanism.[4−7] However, the low power density of LIBs with a graphite anode cannot meet the midterm goal of power battery applications. For improving on the energy storage of the LIBs, great efforts have been paid to explore silicon and tin anodes via a Li alloying mechanism; however, a severe problem facing these materials is the large volume expansion/contraction during alloying and dealloying reaction with Li^+ ions.[8−10] To solve this problem, great efforts have been made in recent years with design of nanostructured materials.[11−16]

Increase in energy density and power density is of great significance for rechargeable LIBs in electric vehicles (EVs) applications. In recent years, oxide intercalation hosts have attracted much attention due to their higher density, leading to larger volumetric energy density, a key parameter for future applications in electronics and electric vehicles.[7] Furthermore, limited global lithium reserves have also challenged the longterm economic viability of large-scale Li-ion energy storage systems.[17] Although $Ti_2Nb_2O_7$ has demonstrated recently a reversible capacity ~280 mAh g^{-1} in the voltage of 1.0−2.5 V as a promising alternative anode for LIBs,[18−20] the price of Nb is cost prohibitive for practical applications. Therefore, searching for low-cost oxide materials free of lithium is still an interesting topic to pursue. A new oxyfluorinated titanium phosphate, $Na_3[Ti_2P_2O_{10}F]$, has been reported by Li et al.[21] The high ionic conductivity of $Na_3[Ti_2P_2O_{10}F]$ is comparable to that of the NASICON-type titanium phosphate.[22] We recently investigated the Na-ion diffusion pathway in $Na_3[Ti_2P_2O_{10}F]$ using temperature-varied neutron powder diffraction (NPD).[23] The NPD results clearly show that Na-ion diffusion paths follow a two-dimensional (2D) trajectory through the *ab* plane.[23] This material is a very ideal ionic insertion/extraction host due to its open framework structure.

Herein, we show $Na_3[Ti_2P_2O_{10}F]$ can function as a low-cost, excellent anode for rechargeable LIBs with a capacity of more than 200 mAh g^{-1} at a 20 mA g^{-1} discharge/charge current rate, as well as excellent cycling and rate capability. The abundant resource of sodium is another advantage of $Na_3[Ti_2P_2O_{10}F]$ compared to other oxide intercalation hosts, like $Li_4Ti_5O_{12}$.

2. EXPERIMENTAL SECTION

2.1. Materials Synthesis. Pure-phase $Na_3[Ti_2P_2O_{10}F]$ was obtained by a hydrothermal method as reported elsewhere.[21,23]

2.2. Characterizations. The morphology of the products was observed by a scanning electron microscope (SEM, Hitachi S-4800). The phases and purity of the products were examined by powder X-ray diffraction (XRD) with a Bruker D8 Advance diffractometer equipped with a Cu Kα radiation source (λ_1 = 1.540 60 Å, λ_2 = 1.544 39 Å) and a

Received: October 27, 2014
Accepted: December 26, 2014
Published: December 26, 2014

DOI: 10.1021/am507272x
ACS Appl. Mater. Interfaces 2015, 7, 1270−1274

LynxEye_XE detector. The powder patterns were refined using TOPAS software based on the Rietveld method.

2.3. Electrochemical Measurements. A slurry of the 70 wt % $Na_3[Ti_2P_2O_{10}F]$ powder with 20 wt % acetylene black and 10 wt % polyvinylidene fluoride (PVDF) is spread onto a Cu foil to prepare working electrodes. The average mass of the active electrode material is ~4 mg. The electrolyte is 1 mol $LiPF_6$ in ethylene carbonate/dimethyl carbonate (1:1 in volume). The coin-type (CR2032) cells were fabricated with pure lithium foil as a counter electrode, and a Celgard polypropylene/polyethylene/polypropylene as a separator in an argon-filled glovebox. Cells were galvanostatically cycled on a Land BT2000 battery test system (Wuhan, China) in a voltage range of 0.02–2.5 V at 25 °C in a constant-temperature oven.

2.4. In Situ XRD Studies. The working electrode was prepared with the method described above. The design of an in situ testing cell is similar to that in the literature.[24] The in situ XRD patterns were collected with an interval of 60 min for each 2θ scan from 10° to 45° during the first discharge/charge cycle at a current rate of 10 mA g^{-1} over a voltage range from 3 to 0 V versus Li/Li^+.

3. RESULTS AND DISCUSSION

3.1. Structure and Morphology of $Na_3[Ti_2P_2O_{10}F]$. Figure 1a shows the Rietveld refinement results of the $Na_3[Ti_2P_2O_{10}F]$. The space group of $Na_3[Ti_2P_2O_{10}F]$ is *I*4/*mmm*, and the refined lattice parameters of the $Na_3[Ti_2P_2O_{10}F]$ sample are a = 6.4447(62) Å and c = 10.6570(11) Å. The refined atomic parameters are listed in Table S1 (Supporting Information). The XRD refinement results are consistent with the neutron diffraction results.[21]

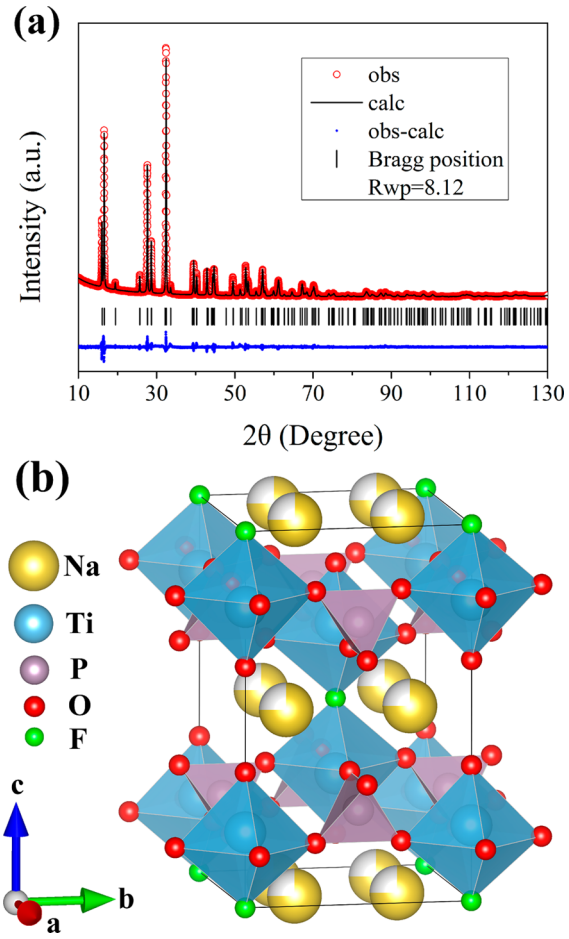

Figure 1. (a) XRD pattern of $Na_3[Ti_2P_2O_{10}F]$ and Rietveld refinement profile. Circles and lines denote the observed and calculated intensities, respectively. The differences between the observed and calculated patterns and the referenced peak positions are also shown at the bottom. (b) Crystal structure of the $Na_3[Ti_2P_2O_{10}F]$.

As shown in Figure 1b, the structure has 4-fold symmetry with the PO_4 tetrahedra and TiO_5F distorted octahedral linked by sharing four oxygen atoms to form an open framework. Meanwhile Na is located at the large interstitial space between the PO_4 tetrahedra and TiO_5F distorted octahedra, and the large interstitial space is beneficial for ion migrations. From Supporting Information, Table S1, the refined results show the occupancy of Na atom is ~0.75, which provides possible sites for Li^+ insertion.

Single-phase $Na_3[Ti_2P_2O_{10}F]\cdot xH_2O$ was obtained after hydrothermal treatment (Supporting Information, Figure S1). As shown in Figure 2, the as-synthesized $Na_3[Ti_2P_2O_{10}F]\cdot xH_2O$ sample shows dispersed cubic crystallites with particle sizes of 1–3 μm. The crystallite demonstrates its growth habit of a 4-fold rotational symmetry under hydrothermal conditions. After calcination, the $Na_3[Ti_2P_2O_{10}F]$ crystallites aggregated, and the sharp edges became blunt, while the cubic morphology was kept well.

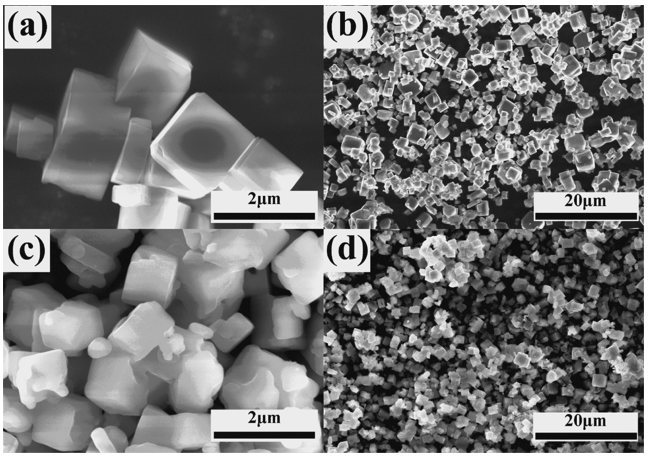

Figure 2. SEM images of the as-synthesized $Na_3[Ti_2P_2O_{10}F]\cdot xH_2O$ (a, b) and the sample after calcined at 550 °C in Ar (c, d).

3.2. Electrochemical Properties of $Na_3[Ti_2P_2O_{10}F]$. The feasibility of the $Na_3[Ti_2P_2O_{10}F]$ as an anode material for LIBs was investigated by galvanostatic charge–discharge testing over a voltage range from 0.02 to 2.5 V. Figure 3a shows typical first three discharge (Li^+ insertion)/charge (Li^+ extraction) curves of a $Na_3[Ti_2P_2O_{10}F]$ electrode at a current density of 20 mA g^{-1}. During discharging, the voltage drops quickly to 1.3 V, and then the curve slopes slowly until the cutoff voltage of 0.02 V. During charging, the curve slopes up to the cutoff voltage of 2.5 V; no obvious plateau appears. The reversible capacity of the $Na_3[Ti_2P_2O_{10}F]$ is ~200 mAh g^{-1} at a current rate of 20 mA g^{-1} (~0.1 C) in the first cycle. After three discharge/charge cycles at low current rate, the cell is tested at a current density of 200 mA g^{-1}. In the fourth cycle the reversible charging capacity of the $Na_3[Ti_2P_2O_{10}F]$ electrode is ~121 mA g^{-1}. Note that a large irreversible capacity loss was observed during the first discharge/charge. The low first-cycle Coulombic efficiency was ascribed to the formation of a solid electrolyte interphase (SEI) layer on the $Na_3[Ti_2P_2O_{10}F]$ surface and possible Li trapping at the anode,[25,26] which can be cured by prelithiation treatment on the anode powder before making the cells.[27] As shown in Figure 3b, the reversible specific capacity

DOI: 10.1021/am507272x
ACS Appl. Mater. Interfaces 2015, 7, 1270–1274

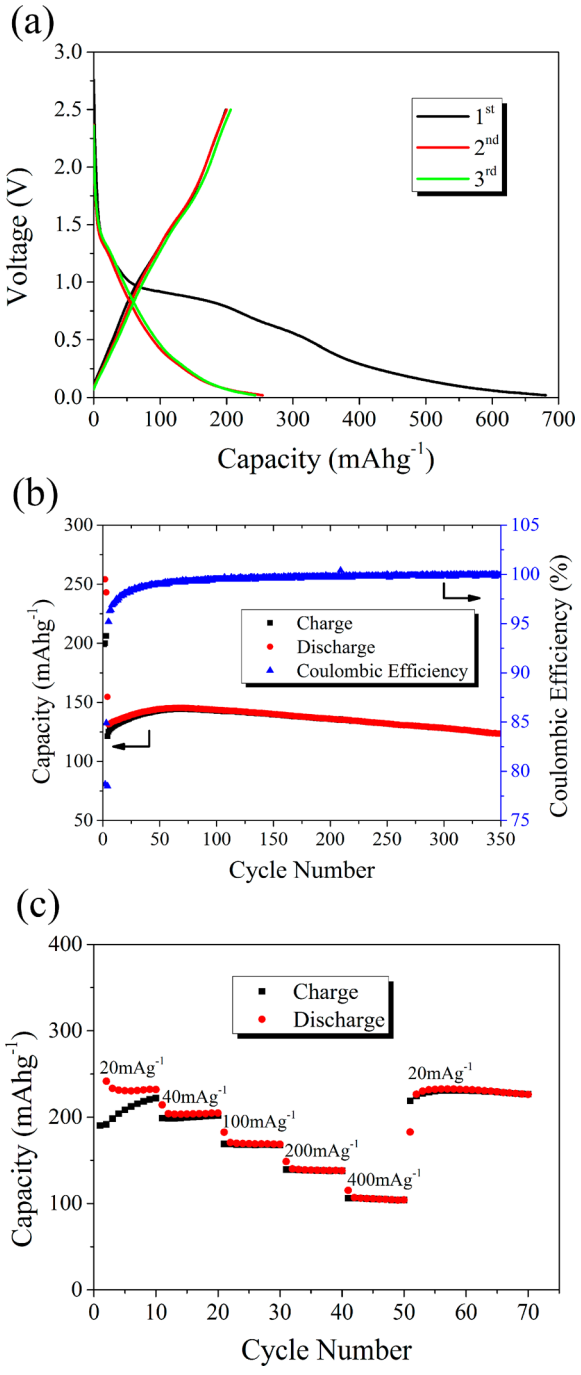

Figure 3. Lithium-ion storage performance of $Na_3[Ti_2P_2O_{10}F]$ electrodes. (a) The first, second, and third discharge/charge curves at a current rate of 20 mA g^{-1} (~0.1 C) in the voltage range from 0.02 to 2.5 V versus Li^+/Li; (b) the capacity and Coulombic efficiency vs cycle number at a current rate of 200 mA g^{-1} (~1 C); (c) the capacity vs cycle number at various current rates.

increases slowly until the 70th cycle, which indicates there is an activation process. For clarity, the data of the first three initial cycles are not included in Figure 2b. The maximum charging capacity reached ~144 mA g^{-1} at a current rate of 200 mA g^{-1} (~1 C). After 350 cycles, the reversible specific capacity remains 123 mA g^{-1}, which is comparable to the fourth cycle. Simultaneously, the Coulombic efficiency increases from 78% in the fourth cycle to 95% in the fifth cycle and keeps further increasing. After roughly 40 cycles, the Coulombic efficiency is above 99% and then stable. The discharge/charge curves in various cycles are shown Supporting Information, Figure S2.

The rate capabilities of the $Na_3[Ti_2P_2O_{10}F]$ electrode were evaluated by discharge/charge at various current densities from 20 mA g^{-1} to 400 mA g^{-1}. As shown in Figure 3c, the reversible specific capacity remains approximately 145 mAh g^{-1} at a discharge/charge rate of 200 mA g^{-1} (~1 C) and 105 mAh g^{-1} at a discharge/charge rate of 400 mA g^{-1} (~2 C), respectively. Importantly, after testing at high current rates, the capacity of the $Na_3[Ti_2P_2O_{10}F]$ electrode tested at a current rate of 20 mA g^{-1} can approach the initial value, indicating its high reversibility.[23] Supporting Information, Figure S3 shows the discharge/charge curves of the 5th, 15th, 25th, 35th, and 45th cycles. With the current density increasing, the polarization becomes larger, which may be caused by the sluggish kinetics of lithium-ion extraction/insertion. These results show that the $Na_3[Ti_2P_2O_{10}F]$ is a potential anode for LIBs.

3.3. Structural Evolution of the $Na_3[Ti_2P_2O_{10}F]$ Electrode upon Cycling. To understand the discharge/charge mechanism of the $Na_3[Ti_2P_2O_{10}F]$ electrode in LIBs, in situ XRD experiments were carried out during the first discharge/charge cycle. From Figure 4a, it can be seen that during lithium-ion insertion/extraction into the $Na_3[Ti_2P_2O_{10}F]$ electrode, all $Na_3[Ti_2P_2O_{10}F]$ peaks remain; however, intensities of some peaks decreased, and no new peaks appear, which indicates a solid solution reaction during discharge/charge. In the first discharge process, the (002) and (013) peaks related to *c*-axis shift to high angle during

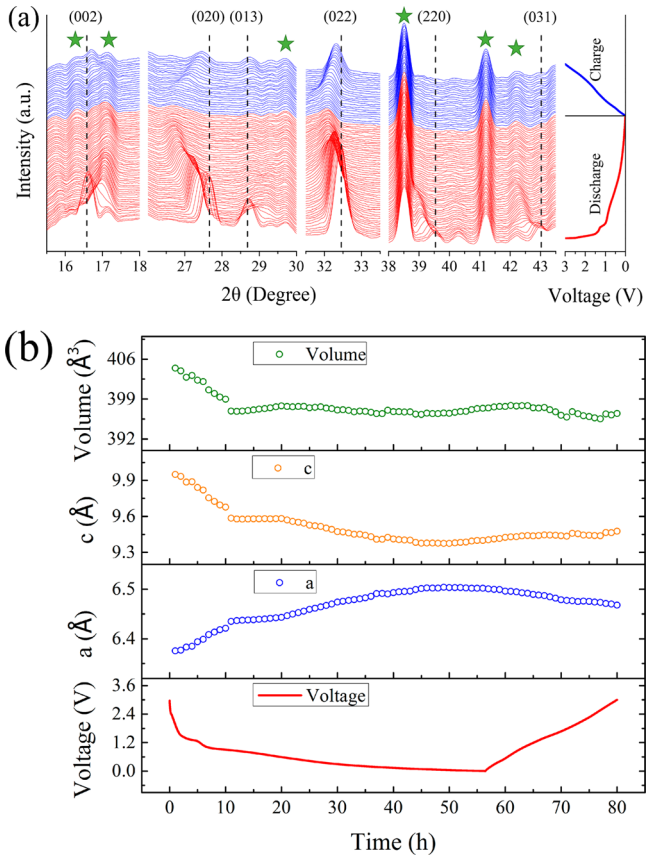

Figure 4. (a) In situ XRD patterns of the $Na_3[Ti_2P_2O_{10}F]$ electrodes with different states of discharge/charge. ☆ denotes the peaks from BeH_2, BeO, and Be; (b) lattice parameters and lattice volume values obtained from in situ XRD refinement result.

DOI: 10.1021/am507272x
ACS Appl. Mater. Interfaces 2015, 7, 1270−1274

discharging and move backward during charging. The (020) peak related to *a*-axis shift to low angle during discharging and move backward during charging. However, some peaks were not observed after charging because the intensity of those peaks is too low to distinguish, such as (220) and (031).

To precisely examine the changes of lattice parameters and volume during Li-ion insertion/extraction into the lattice, the lattice parameters were calculated from in situ XRD patterns and plotted in Figure 4b. During discharging process, the *a*-axis length increases, while the *c*-axis length decreases. The cell volume drops at the beginning of discharging, and then it keeps constant in the following tests. After charging, the lattice parameters cannot recover to the initial value.

4. CONCLUSIONS

In summary, we have successfully prepared the $Na_3[Ti_2P_2O_{10}F]$ by a hydrothermal method and evaluated its feasibility as an anode material for LIBs. $Na_3[Ti_2P_2O_{10}F]$ exhibits a reversible capacity of more than 200 mAh g^{-1} at 20 mA g^{-1} (~0.1 C) discharge/charge rate and 105 mA g^{-1} at 400 mA g^{-1} (~2C) discharge/discharge rate with a lower intercalation voltage. The result of in situ XRD test shows the structural evolution during discharge/charge. The structure of $Na_3[Ti_2P_2O_{10}F]$ was kept during discharge/charge, which indicates a solid solution behavior. After the first charging, the lattice parameters cannot recover to the initial value. $Na_3[Ti_2P_2O_{10}F]$ also shows excellent cycling stability and rate capability, making it a potential anode for lithium-ion batteries.

■ ASSOCIATED CONTENT

Supporting Information

The refined structure parameters for $Na_3[Ti_2P_2O_{10}F]$, XRD pattern, and the charge/discharge curves. This material is available free of charge via the Internet at http://pubs.acs.org.

■ AUTHOR INFORMATION

Corresponding Author

*Phone: +86-10-82649901. Fax: +86-10-82649046. E-mail: csun@iphy.ac.cn.

Notes

The authors declare no competing financial interest.

■ ACKNOWLEDGMENTS

C.S. gratefully acknowledges the finacial support of the National Science Foundation of China (NSFC) (Grant Nos. 51372271, 51172275). The work of Y.K. was supported by the Creativity and Innovation Project Fund (1,140009,01) of Ulsan National Institute of Science and Technology.

■ REFERENCES

(1) Armand, M.; Tarascon, J. M. Building Better Batteries. *Nature* **2008**, *451*, 652−657.
(2) Goodenough, J. B.; Kim, Y. Challenges for Rechargeable Li Batteries. *Chem. Mater.* **2010**, *22*, 587−603.
(3) Sun, C.; Rajasekhara, S.; Goodenough, J. B.; Zhou, F. Monodisperse Porous $LiFePO_4$ Microspheres for a High Power Li-ion Battery Cathode. *J. Am. Chem. Soc.* **2011**, *133*, 2132−2135.
(4) Tarascon, J. M.; Guyomard, D. The $Li_{1+x}Mn_2O_4$/C Rocking-chair System: A Review. *Electrochim. Acta* **1993**, *38*, 1221−1231.
(5) Guyomard, D.; Tarascon, J. M. The Carbon $Li_{1+x}Mn_2O_4$ System. *Solid State Ionics* **1994**, *69*, 222−237.
(6) Ohzuku, T.; Ueda, A.; Nagayama, M.; Iwakoshi, Y.; Komori, H. Comparative-study of $LiCoO_2$, $LiNi_{1/2}Co_{1/2}O_2$ and $LiNiO_2$ for 4-V Secondary Lithium Cells. *Electrochim. Acta* **1993**, *38*, 1221−1231.
(7) Armstrong, A. R.; Lyness, C.; Panchmatia, P. M.; Islam, M. S.; Bruce, P. G. The Lithium Intercalation Process in the Low-voltage Lithium Battery Anode $Li_{1+x}V_{1-x}O_2$. *Nat. Mater.* **2011**, *10*, 223−229.
(8) Winter, M.; Besenhard, J. O.; Spahr, M. E.; Novak, P. Insertion Electrode Materials for Rechrageable Lithium Batteries. *Adv. Mater.* **1998**, *10*, 725−763.
(9) Li, H.; Wang, Z.; Chen, L.; Huang, X. Resaerch on Advanced Materials for Li-ion Batteries. *Adv. Mater.* **2009**, *21*, 4593−4607.
(10) Kasavajjula, U.; Wang, C.; Appleby, A. J. Nano- and Bulk-silicon-based Insertion Anodes for Lithium-ion Secondary Cells. *J. Power Sources* **2007**, *163*, 1003−1039.
(11) Li, H.; Huang, X.; Chen, L.; Wu, Z.; Liang, Y. A High Capacity Nano-Si Composite Anode Material for Lithium Rechargeable Batteries. *Electrochem. Solid-State Lett.* **1999**, *2*, 547−549.
(12) Chan, C. K.; Peng, H. L.; Liu, G.; McIlwarth, K.; Zhang, X. F.; Huggins, R. A.; Cui, Y. High-performance Lithium Battery Anodes Using Silicon Nanowires. *Nat. Nanotechnol.* **2008**, *3*, 31−35.
(13) Park, M.; Kim, M.; Joo, J.; Kim, K.; Kim, J.; Ahn, S.; Cui, Y.; Cho, J. Silicon Nanotube Battery Anodes. *Nano Lett.* **2009**, *9*, 3844−3847.
(14) Idota, Y.; Kubota, T.; Matsufuji, A.; Maekawa, Y.; Miyasaka, T. Tin-based amorphous oxide: A High-capacity Lithium-ion-storage Materials. *Science* **1997**, *276*, 1395−1397.
(15) Lou, X. W.; Wang, Y.; Yuan, C.; Lee, J. Y.; Archer, L. A. Template-free Synthesis of SnO_2 Hollow Nanostructures with High Lithium Storage Capacity. *Adv. Mater.* **2006**, *18*, 2325−2329.
(16) Lee, K. T.; Jung, Y. S.; Oh, S. M. Synthesis of Tin-encapsulated Spherical Hollow Carbon for Anode Material in Lithium Secondary Batteries. *J. Am. Chem. Soc.* **2003**, *125*, 5652−5653.
(17) Ellis, B. L.; Makahnouk, W. R. M.; Makimura, Y.; Toghill, K.; Nazar, L. F. A Multifunctional 3.5V Iron-based Phosphate Cathode for Rechargeable Batteries. *Nat. Mater.* **2007**, *6*, 749−753.
(18) Han, J. T.; Huang, Y. H.; Goodenough, J. B. New Anode Framework for Rechargeable Lithium Batteries. *Chem. Mater.* **2011**, *23*, 2027−2029.
(19) Han, J. T.; Goodenough, J. B. 3-V Full Cell Performance of Anode Framework $TiNb_2O_7$/spinel $LiNi_{0.5}Mn_{1.5}O_4$. *Chem. Mater.* **2011**, *23*, 3404−3407.
(20) Guo, B.; Yu, X.; Sun, X.; Chi, M.; Qiao, Z.; Liu, J.; Hu, Y.; Yang, X.; Goodenough, J. B.; Dai, S. A Long-life Lithium-ion Battery with Highly Porous $TiNb_2O_7$ Anode for Large-scale Electrical Energy Storage. *Energy Environ. Sci.* **2014**, *7*, 2220−2226.
(21) Yang, S.; Li, G.; You, L.; Tao, J.; Loong, C.; Tian, S.; Liao, F.; Lin, J. $Na_3[Ti_2P_2O_{10}F]$: A New Oxyfluorinated Titanium Phosphate with an Ionic Conductive Property. *Chem. Mater.* **2007**, *19*, 942−947.
(22) Mouahid, F. E.; Bettach, M.; Zahir, M.; Maldonado-Manso, P.; Bruque, S.; Losilla, E. R.; Aranda, M. A. G. Crystal chemistry and ion conductivity of the $Na_{1+x}Ti_{2-x}Al_x(PO_4)_3$ ($0 \le x \le 0.9$) NASICON series. *J. Mater. Chem.* **2000**, *10*, 2748−2753.
(23) Ma, Z.; Wang, Y.; Sun, C.; Alonso, J. A.; Fernández-Díaz, M. T.; Chen, L. Q. Experimental visualization of the diffusion pathway of sodium ions in the $Na_3[Ti_2P_2O_{10}F]$ anode for sodium-ion batteries. *Sci. Reports* **2014**, *4*, 7231.
(24) Sathiya, M.; Ramesha, K.; Rousse, G.; Foix, D.; Gonbeau, D.; Prakash, A. S.; Doublet, M. L.; Hemalatha, K.; Tarascon, J. M. High performance $Li_2Ru_{1-y}Mn_yO_3$ ($0.2 \le y \le 0.8$) cathode materials for rechargeable lithium-ion batteries: their understanding. *Chem. Mater.* **2013**, *25*, 1121−1131.
(25) Wu, H.; Zhang, G.; Liu, N.; Carney, T. J.; Yang, Y.; Cui, Y. Engineering empty space between Si nanoparticles for lithium-ion battery anodes. *Nano Lett.* **2012**, *12*, 904−909.
(26) Pan, H.; Lu, X.; Yu, X.; Hu, Y.; Li, H.; Yang, X.; Chen, L. Sodium Storage and Transport Properties in Layered $Na_2Ti_3O_7$ for Room-temperature Sodium-ion Battery. *Adv. Energy Mater.* **2013**, *3*, 1186−1194.

DOI: 10.1021/am507272x
ACS Appl. Mater. Interfaces 2015, 7, 1270−1274

(27) Zhao, J.; Lu, Z.; Liu, N.; Lee, H.; McDowell, M. T.; Cui, Y. Dry-air-stable Lithium Silicide-lithium Oxide Core-shell Nanoparticles as High-capacity Prelithiation Reagents. *Nat. Commun.* **2014**, *5*, 5088.

DOI: 10.1021/am507272x
ACS Appl. Mater. Interfaces 2015, 7, 1270−1274